Giant tunnel magnetoresistance in two-dimensional van der Waals magnetic tunnel junctions: $Ag/CrI_3/MoSi_2N_4/CrI_3/Ag$

Hao Liu,[1,2] Pan Wang,[1,2] Yixin Zong,[3] Hongyu Wen,[1,*] Yue-Yang Liu,[1,†] and Jianbai Xia[1,2]

[1]*State Key Laboratory of Superlattices and Microstructures, Institute of Semiconductors, Chinese Academy of Sciences, Beijing 100083, China*

[2]*Center of Materials Science and Optoelectronics Engineering, University of Chinese Academy of Sciences, Beijing 100083, China*

[3]*Bureau of Frontier Sciences and Education, Chinese Academy of Science, Beijing 100864, China*

(Received 18 March 2022; revised 29 August 2022; accepted 13 September 2022; published 26 September 2022)

With intrinsic magnetism, two-dimensional (2D) CrI_3 has attracted tremendous interest because of the potential application in magnetic devices of smaller size. We propose to use 2D $MoSi_2N_4$ material, which has remarkable stability, excellent electronic properties, and high mobility, as tunnel barrier in vertical magnetic tunnel junction (MTJ), and demonstrate that it is able to generate a giant tunnel magnetoresistance (TMR) over $10^5\%$ when integrated with CrI_3 ferromagnetic layers and Ag electrodes. Combining with density-functional theory and nonequilibrium Green's function approach, we systematically investigate the electron transmission, band structures, and projected local density of states and elaborate the transmission mechanism. The TMR and spin injection efficiency maintain high values below 0.25 V. These results indicate that $MoSi_2N_4$ is a promising barrier material in future 2D vertical MTJs and provide important guidance for designing devices.

DOI: 10.1103/PhysRevB.106.104429

I. INTRODUCTION

Magnetic tunnel junction (MTJ), which consists of a nonferromagnetic insulating tunnel barrier sandwiched between two ferromagnetic layers, has important technological applications, such as spin-transfer-torque magnetic random-access memory [1,2] and spin-torque diodes [3]. Traditional MTJs are verified to have huge tunnel magnetoresistance (TMR) with MgO [4] and AlO_x [5] (1.8–2.5 nm) as tunnel barrier, CoFeB [6] and Fe [7] as ferromagnetic layers. However, the interfaces of metal oxides and metals are prone to present nonuniform thicknesses, pinholes, and defects during preparation of the thin films [8]. As a result, it is difficult to keep the stability and performance of MTJs based on traditional technology when decreasing the size of devices. The development of two-dimensional (2D) materials provides new choices for the components in MTJs. Two-dimensional materials have smooth interfaces without dangling bond, and thus can be achieved by epitaxial growth on substrate layer by van der Waals force. Two-dimensional MTJs, which are actually 2D heterostructures, possess better layered interface structure than traditional MTJs, hence better electrical properties, and more stable performances at a smaller size.

Intrinsic magnetism has been discovered in 2D crystal, such as monolayer CrI_3 [9], triggering a series of research and thinking [10–13]. CrI_3 can maintain magnetic long-range order even in a single layer, which has a magnetic easy axis out of plane. Two-dimensional ferromagnetic materials with out-of-plane magnetism are vital to decrease the thickness of MTJs and increase the storage density. It is found that the TMR can reach 19 000% in multiple spin-filter MTJ based on four-layer CrI_3 [13], which shows that CrI_3 is of high research value for memory devices.

Apart from ferromagnetic layers, barrier material has a big impact on the transmission of MTJs. Graphene [14] and hexagonal boron nitride (hBN) [8] are normal barrier materials in 2D MTJs, but the TMR is usually low in theory or in the laboratory [15,16]. Therefore, a new 2D barrier is important for the progress of MTJ technology. In our work, we employ CrI_3 as ferromagnetic layers to construct MTJs with different 2D tunnel barrier, including hBN, graphene, and $MoSi_2N_4$. $MoSi_2N_4$ is a 2D large-area semiconducting material (band gap $\sim$1.94 eV) with high strength ($\sim$66 GPa), remarkable stability, excellent electronic properties, and high mobility [17], which is well suited as tunnel barrier in MTJ. In this paper, we propose to apply $MoSi_2N_4$ as tunnel barrier between CrI_3 layers to construct vertical MTJ device, which effectively reduces the thickness of the device, and obtain a giant TMR of over $10^5\%$ by *ab initio* calculations. $MoSi_2N_4$ was employed as tunnel barrier in planar MTJ device in the previous studies [18], whereas the vertical structures we studied are easier to obtain in the laboratory and have a better interface quality. The underlying mechanism of the giant TMR is analyzed by the band structures and electron transmission.

II. METHODS AND MODEL

In order to establish the device models, we first constructed the interface of the var der Waals heterostructures and then did the optimizations and electronic transport calcula-

*wenhongyu@semi.ac.cn
†yueyangliu@semi.ac.cn

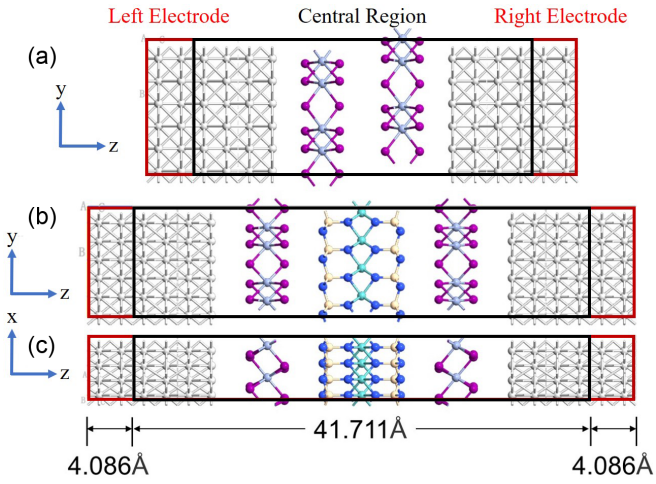

FIG. 1. (a) Structure of the MTJ model Ag/bilayer CrI_3/Ag. (b), (c) Structure of the MTJ model Ag/CrI_3/$MoSi_2N_4$/CrI_3/Ag from different perspective, where the thickness of the barrier $MoSi_2N_4$ is about 10 Å. Red squares represent electrodes and black squares represent central regions in devices.

tions of devices by ATOMISTIX TOOLKIT (QUANTUM ATK) [19] based on the density-functional theory (DFT) and nonequilibrium Green's function (NEGF) approach [20]. The density mesh cutoff was 105 hartree and geometry optimization force was 0.01 eV/Å. The generalized gradient approximation–Perdew-Burke-Ernzerhof [21] formalism was used to express exchange and correlation functional. The simulations were performed at 0 K. The Monkhorst-Pack k-point grids were 98×57 in transport calculations. The band structures were obtained in Vienna *Ab initio* Simulation Package (VASP) [22] with projector augmented-wave method and plane-wave basis set. A kinetic energy cutoff of 400 eV is used in the calculations.

CrI_3 bilayer shows ferromagnetic spin aligns within each layer, but exhibits antimagnetic property between the layers [12], which makes CrI_3 bilayer able to form spin-filtering device. The interlayer antimagnetism decouples the magnetism of each layer, so the magnetism of the monolayer can be flipped independently. We first establish the MTJ model consisted of CrI_3 bilayer and Ag electrodes, which have a low Schottky barrier with layered CrI_3 [23], at sides [Fig. 1(a)]. The device has two semi-infinite electrodes on both sides and one central scattering region in the middle, and electrons will transport along the z axis in simulation. Then, we tried different 2D barrier (hBN, graphene, and $MoSi_2N_4$ [Figs. 1(b) and 1(c)] between CrI_3 bilayer to construct MTJs. In the circumstances, the two CrI_3 layers are stacked differently from the bilayer without barrier after sufficient optimization because the barrier changes the interaction between layers. The lattice mismatch between CrI_3 and Ag is 5%, and between $MoSi_2N_4$ and Ag is 4.5%.

III. RESULTS AND DISCUSSION

Through changing the magnetic moment of ferromagnetic layer (CrI_3), we get the transmission spectra at zero bias of all the MTJs under parallel and antiparallel magnetization configurations (PC and APC). Conductances can be derived from the transmission probabilities by Landau formula: $G_\sigma = \frac{e^2}{h}\sum_{k_{//},j} T^+(k_{//}, j)$ and $G = G_\uparrow + G_\downarrow$, where σ indicates the spin $\uparrow$ and $\downarrow$, $k_{//}$ indicates the horizontal momentum on the plane perpendicular to the direction of transmission, j represents the corresponding Bloch state, and T^+ is the transmission probability along positive direction. The conductance of each MTJ is represented by G_P (conductance under PC) and G_{AP} (conductance under APC), exhibited in Table I. TMR is defined as $\mathrm{TMR} = (G_P - G_{AP})/G_{AP} \times 100\%$, which is exhibited in column 3 in Table I. It can be seen from the table that the MTJ based on CrI_3 bilayer with no barrier shows a TMR of 2303.1%, which is obviously smaller than the MTJ with a barrier, indicating that the barrier plays an important role in the transmission. We increased the number of layers of barrier hBN and graphene to avoid the influence of barrier thickness. The calculated TMR of the MTJ with $MoSi_2N_4$ barrier has a giant value over 10^5% around zero bias, which is much larger than the previous 2D vertical MTJs.

We analyzed the causes of the giant TMR from transmission spectra first. The transmission spectra of the structure Ag/CrI_3/$MoSi_2N_4$/CrI_3/Ag are shown in Figs. 2(a)–2(d), which represent the transmission of the majority or minority spin under PC or APC, respectively. In the transmission spectra, the horizontal/vertical axis represents k value along the x- and y axes (k_x/k_y) of the device, and the colors indicate transmission probabilities. The spectrum of majority spin under PC [Fig. 2(a)] is significantly different from minority spin: Quantitatively, the highest transmission probability of majority-spin electrons is almost 1, but of minority-spin electrons is 0.15. What is more, majority-spin electrons have obvious high transmission in many areas but minority spin electrons are only allowed to transport in a few areas. On the other hand, the transmission spectra under APC [Figs. 2(c) and 2(d)] show low transmission, the maximum probability of which is no more than 5×10^{-4}. The spectra demonstrate that the electric current under PC is much larger than that under APC, leading to a giant TMR and high spin injection efficiency (SIE).

The symmetries of the dominant transmission electrons could be obtained from the spectra through the hot spots, which are the spots with the largest transmission probability in a spectrum. The tunneling electrons in MTJs are usually divided into $\Delta_1(s, p_z, d_{z^2})$ with spherical symmetry, $\Delta_5(p_x, p_y, d_{xz}, d_{yz})$ with twofold symmetry, $\Delta_2(d_{x^2-y^2})$ and $\Delta_{2'}(d_{xy})$ with other symmetries according to their symmetries because of their similar transmission performance.

Figure 2(a) is the transmission spectrum of majority-spin electrons under PC, which has the strongest transmission of the four circumstances. The hot spots are circled in red, located around $k_y = 0$ (x-) axis and $k_x = 0$ (y-) axis, meaning that the Δ_5 or Δ_2 electrons lead the charge transfer of the MTJ, because the high transmission region of Δ_1 electrons should distribute near the origin and $\Delta_{2'}$ electrons should distribute near the diagonals of axis. The types of dominating transmission electrons could be derived from the transmission eigenstates [Figs. 2(e) and 2(f)] further. We found the hot spots have different transmission eigenstates near x- (Fig. 2(a): spot 1–4) and y axes (Fig. 2(a): spot

TABLE I. Calculated conductance (Siemens) of the parallel (G_P, column 2) and antiparallel (G_{AP}, column 5) channels of the MTJs based on CrI_3 ferromagnetic layers with different barriers. The spin-resolved conductance is given in the table (conductance of majority/minority spin of parallel channels is in columns 3, 4 and of antiparallel channels is in columns 6, 7). Their TMR values are shown in the last column. The structures have been optimized sufficiently.

Barrier material	G_P	Majority	Minority	G_{AP}	Majority	Minority	TMR (%)
No barrier	7.70×10^{-06}	7.66×10^{-06}	3.43×10^{-08}	3.20×10^{-07}	1.62×10^{-07}	1.59×10^{-07}	2 303.10
hBN	2.20×10^{-06}	2.05×10^{-06}	1.52×10^{-07}	2.92×10^{-08}	1.46×10^{-08}	1.46×10^{-08}	7 434.36
Two-layer hBN	2.44×10^{-07}	2.22×10^{-07}	2.17×10^{-08}	8.35×10^{-10}	4.17×10^{-10}	4.17×10^{-10}	29 089.82
Three-layer hBN	8.45×10^{-09}	8.24×10^{-09}	2.14×10^{-10}	3.74×10^{-11}	1.87×10^{-11}	1.87×10^{-11}	22 482.26
Graphene	6.29×10^{-06}	6.25×10^{-06}	3.40×10^{-08}	3.50×10^{-08}	1.75×10^{-08}	1.75×10^{-08}	17 842.97
Two-layer graphene	7.72×10^{-07}	7.05×10^{-07}	6.70×10^{-08}	9.74×10^{-08}	4.87×10^{-08}	4.87×10^{-08}	693.32
Three-layer graphene	2.00×10^{-07}	1.83×10^{-07}	1.71×10^{-08}	3.05×10^{-08}	1.52×10^{-08}	1.53×10^{-08}	557.25
$MoSi_2N_4$	1.75×10^{-07}	1.71×10^{-07}	3.52×10^{-09}	1.60×10^{-10}	8.07×10^{-11}	7.97×10^{-11}	108 974.89

5–8), respectively. The transmission eigenstates mainly distribute around chromium atoms of CrI_3, meaning that CrI_3 plays a leading role in electron transfer. Also, the eigenstates have four nodes, which is a typical characteristic of d electrons. The difference is that the four nodes locate at x- and z axes in Fig. 2(e) but y- and z axis in Fig. 2(f), which indicates the orbitals of high transmission electrons are d_{xz} and d_{yz}, respectively. As a result, it can be confirmed that the dominant electrons in transmission under PC are Δ_5 electrons, or more specifically, d_{xz} and d_{yz} electrons. Δ_5 electrons of majority spin show high transmission probabilities under PC, which does not appear in other spectra, and that is an important cause of giant TMR.

After confirming the type of dominant electrons in transmission of $Ag/CrI_3/MoSi_2N_4/CrI_3/Ag$, we studied the band structures of the barrier materials in Table I to find the unique property of $MoSi_2N_4$ in CrI_3-based vertical MTJs. We designed a vertical MTJ with transmission along out-of-plane direction, so we hoped to know the band structures along Γ to Z to explore the transmission performance of $MoSi_2N_4$ and CrI_3. However, $MoSi_2N_4$ and CrI_3 are monolayer in the device so there are only some energy levels along Γ to Z. For calculating the transmission direction, the bulk materials of $MoSi_2N_4$ and CrI_3 are utilized in calculations to explore the characteristics along the transport direction.

Figure 3(a) is the band structure of $MoSi_2N_4$ in the MTJ, where $\Gamma \rightarrow Z$ represents the transmission direction in the device. Projected bands of Δ_1, Δ_5, Δ_2, and $\Delta_{2'}$ are symbolized by blue, red, green, and purple squares. Transmission of electrons is our major study object, so we focus on the conduction band in transmission direction ($\Gamma \rightarrow Z$). The conduction-band minimum (CBM) in $\Gamma \rightarrow Z$ is dominated by Δ_5 electrons, which means Δ_5 electrons have the best transmission performance in $\Gamma \rightarrow Z$, and other electrons would be scattered relatively more strongly. It means that $MoSi_2N_4$ material does not affect the high transmission of Δ_5 electrons

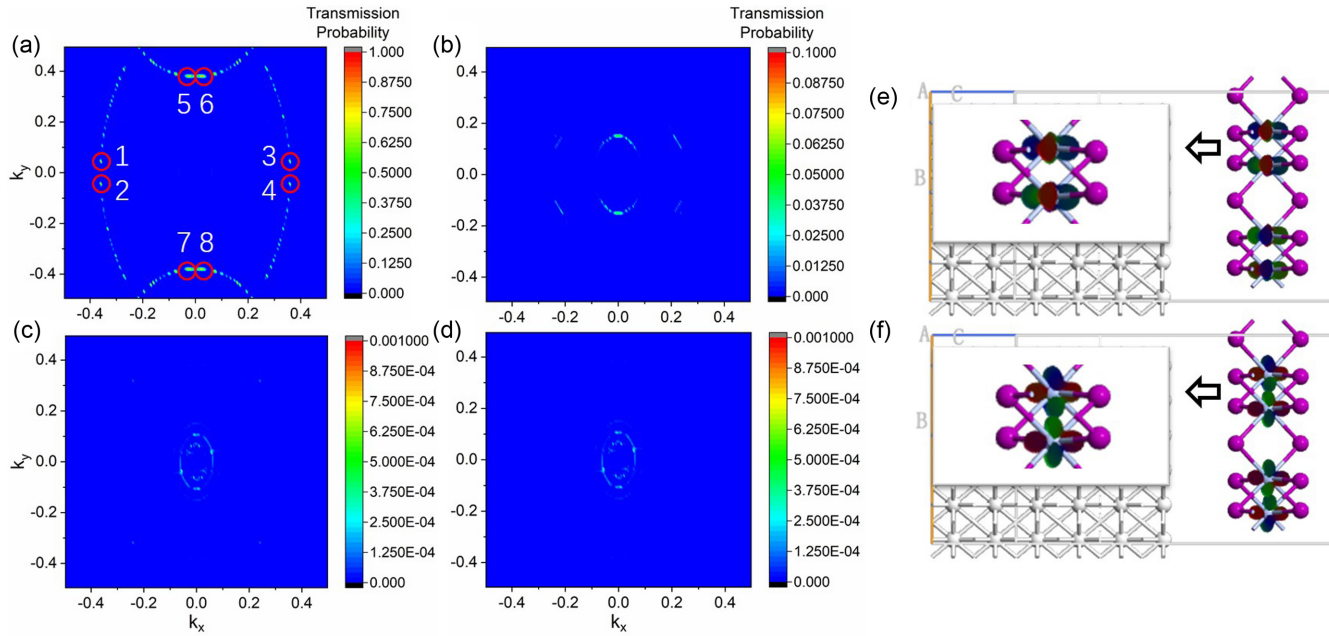

FIG. 2. (a) Majority-spin transmission states and (b) Minority-spin transmission states in parallel magnetization configurations; (c) Majority-spin transmission states and (d) Minority-spin transmission states in antiparallel magnetization configuration. Hot spots are marked by red circles; (e), (f) Transmission eigenstates of the hot spots: (e) spot 1–4; (f) spot 5–8 in Fig. 2(a).

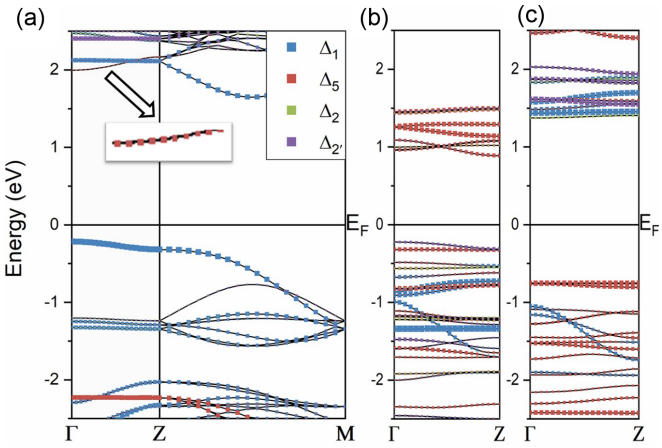

FIG. 3. (a) Band structure of monolayer $MoSi_2N_4$, where Γ, Z, and M indicate (0,0,0), (0,0,0.5), and (0.5,0.5,0) in k space; E_F indicates Fermi surface. Different colors represent the projections of electrons in different symmetries. (b), (c) Band structure of majority- and minority-spin electrons in layered CrI_3.

under PC while assisting with the electron filtration under APC, which is also an important factor in the giant TMR. The band structures of CrI_3 are also exhibited in Figs. 3(b) (majority spin) and 3(c) (minority spin), where $\Gamma \rightarrow Z$ remains the transmission direction. The band gaps of the two spins have a significant difference, showing that CrI_3 is a magnetic material. Figure 3(b) shows a smaller gap and lower CBM, indicating that the spin in Fig. 3(b) is the majority spin of CrI_3 while Fig. 3(c) is the minority. The band gap in Fig. 3(b) is about 1.2 eV, which is consistent with former experiments and calculations [24–26]. The Δ_5 electrons take the largest proportion at CBM in majority spin, which is not in minority spin, further supporting previous conclusions.

For comparison, we have calculated transmission spectra and barrier band structures of all the devices in Table I, and the diagrams are exhibited in the Supplemental Material [27]. Figures S1, S2, and S3 show the transmission spectra of Ag/bilayer CrI_3/Ag, Ag/CrI_3/hBN/CrI_3/Ag, and Ag/CrI_3/graphene/CrI_3/Ag respectively. The primary distinction between the three devices and Ag/CrI_3/$MoSi_2N_4$/CrI_3/Ag is that the transmission of majority spin under PC is relatively more

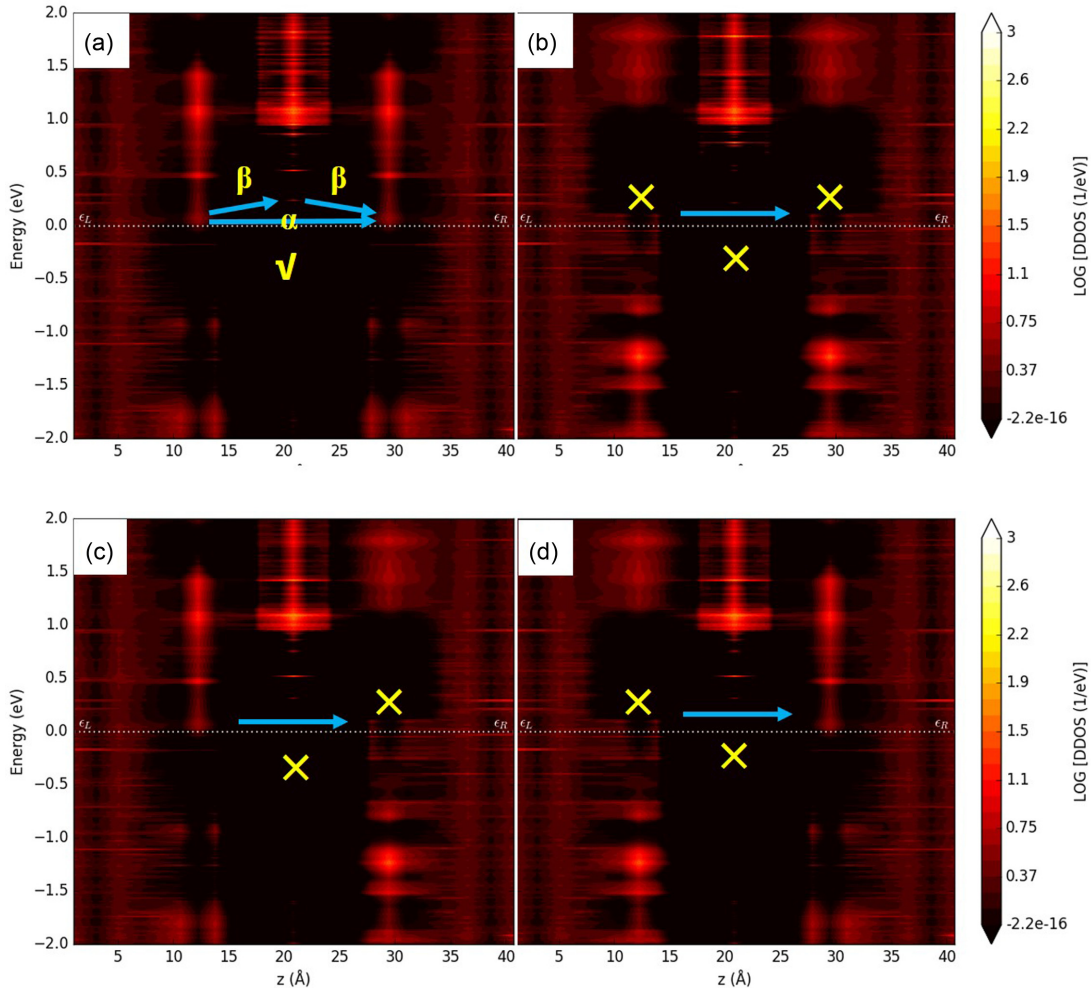

FIG. 4. PLDOS of the majority and minority spin under PC (a), (b) and APC (c), (d) at zero bias. The horizontal axis represents different locations of z axis of the device and the vertical axis represents electron energy. Red color indicates high density of states. The dashed white line represents Fermi level. Blue arrows indicate possible transmission.

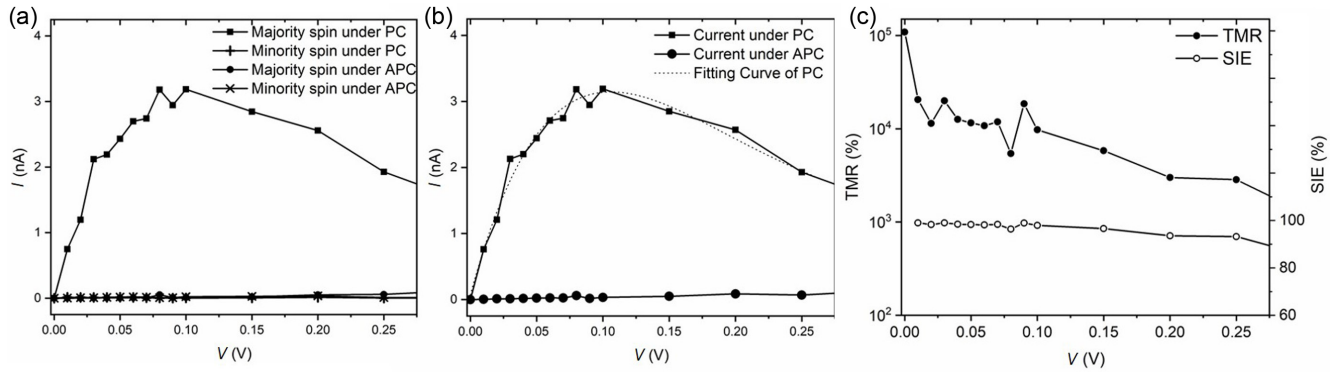

FIG. 5. (a). Spin-resolved $I-V$ characteristic curves in PC and APC. Different curves are labeled by different symbols; (b) Summed $I-V$ characteristic curves in PC (squares) and APC (circles). The imaginary line is the fitting curve of current under PC; (c) TMR (solid circles) and SIE (empty circles) in different voltages.

chaotic, lacking effective filtering of transmitted electrons. In addition, the transmission probabilities under APC of the three devices are not as low as the $MoSi_2N_4$-based device. Therefore, the three devices have smaller TMR. Analyzing from the perspective of band structures (Fig. S4 [27]), it can be found that the CBM in $\Gamma \rightarrow Z$ of hBN bands [Fig. S4(a)] is mostly Δ_1 electrons, and so do the graphene bands [Fig. S4(b)], indicating high transmission of Δ_1 electrons. Different from hBN and graphene, the unique high transmission of Δ_5 electrons of $MoSi_2N_4$ is advantageous in the giant TMR.

The tunneling current is decided by several factors, including tunneling barrier, tunneling distance, tunneling channel number, and density of electronic states (DOS). Figures 4(a)–4(d) give the projected local DOS (PLDOS) diagrams of majority/minority spin under PC/APC in $Ag/CrI_3/MoSi_2N_4/CrI_3/Ag$. The horizontal axis represents the distance from the left electrode in the device. The band alignments could be obtained from the PLDOS. States of $MoSi_2N_4$ monolayer are in the middle and Ag electrodes are on both sides. Between them are CrI_3 layers and Cr atoms located at about 12 and 29 Å, respectively. On account of the existence of Ag metal electrodes, the Fermi level of the device is near the CBM of majority-spin electrons in CrI_3 in Fig. 4(a). The following points can be obtained from Fig. 4(a): First, it can be seen that there are very large DOS near the Fermi level at both sides of the device including CrI_3 layers, which is very beneficial for electron tunneling. Second, the tunneling barrier, i.e., the energy difference between $MoSi_2N_4$ CBM and the Fermi level, is as small as 0.2 eV. This again facilitates the direct tunneling current (arrow α). The $MoSi_2N_4$ CBM could even serve as a second channel for electron transport (arrow β). Finally, the $MoSi_2N_4$ is only about 10 Å in thickness. The electron tunneling across 10-Å distance has been widely observed in different devices [28,29].

Compared with Fig. 4(a) (majority spin under PC), the other three circumstances do not show good transmission. The DOS around Fermi level of both CrI_3 layers in Fig. 4(b), right CrI_3 layer in Fig. 4(c), and left CrI_3 layer in Fig. 4(d) are small. As a result, the transmission is weak, which is consistent with the transmission spectra in Figs. 2(a)–2(d): Only majority spin under PC shows high transmission.

In order to explore the potential in applications of the device $Ag/CrI_3/MoSi_2N_4/CrI_3/Ag$, the transmission spectra at nonzero bias are calculated by NEGF approach to obtain the transport performance. Figure 5(a) shows the currents of majority/minority spin under PC/APC, named as I_P^+, I_P^-, I_{AP}^+, and I_{AP}^- respectively. With the increasing of voltage, only I_P^+ shows a noticeable rise, while the other three currents remain more or less unchanged. On that basis, the current under PC (I_P), equal to I_P^+ plus I_P^-, and under APC (I_{AP}), equal to I_{AP}^+ plus I_{AP}^- could be obtained; then the TMR and SIE:

$$\begin{aligned} \mathrm{TMR} &= (G_P - G_{AP})/G_{AP} \times 100\% \\ &= (I_P - I_{AP})/I_{AP} \times 100\%, \\ \mathrm{SIE} &= (I_P - I_{AP})/(I_P + I_{AP}) \times 100\%. \end{aligned}$$

I_P and I_{AP} are exhibited in Fig. 5(b). There is a considerable difference between I_P and I_{AP} within the bias of 0.25 V. Particularly, the I_P from 0.1 to 0.25 V exhibits an effect of negative differential resistance, but a large gap with I_{AP} still remains. The causes of negative differential resistance are beyond the scope of our discussions in this paper, while the TMR and SIE are the points we are concerned with, shown in Fig. 5(c). At zero bias, TMR of the device could achieve 10^5%, and it is able to keep a value about 10^4% within 0.1 V, and remains about 3000% at 0.25 V. SIE of the device is more than 95% within 0.2 V. It is proved that $Ag/CrI_3/MoSi_2N_4/CrI_3/Ag$ structure has a giant TMR and high SIE in theory, revealing its enormous potential in applications.

We have calculated the PLDOS diagrams of finite bias to explain the transport performance. The PLDOS diagrams of majority/minority spin under PC/APC at 0.05 V are exhibited in Figs. 6(a)–6(d), respectively. The PLDOS at other biases (0.10, 0.15, and 0.20 V) are provided in the Supplemental Material (Figs. S5, S6, and S7 [27]). With the increasing of the bias voltage, the Fermi level of the left electrode (ϵ_L) decreases, and the Fermi level of the right electrode (ϵ_R) increases. Besides, the band alignments are very similar with zero bias in Fig. 4. There are large DOS near Fermi level at both CrI_3 layers in Fig. 6(a); thus, the electron tunneling from the left CrI_3 to the right one is large. In contrast, for the minority spin under PC shown in Fig. 6(b), the DOS near

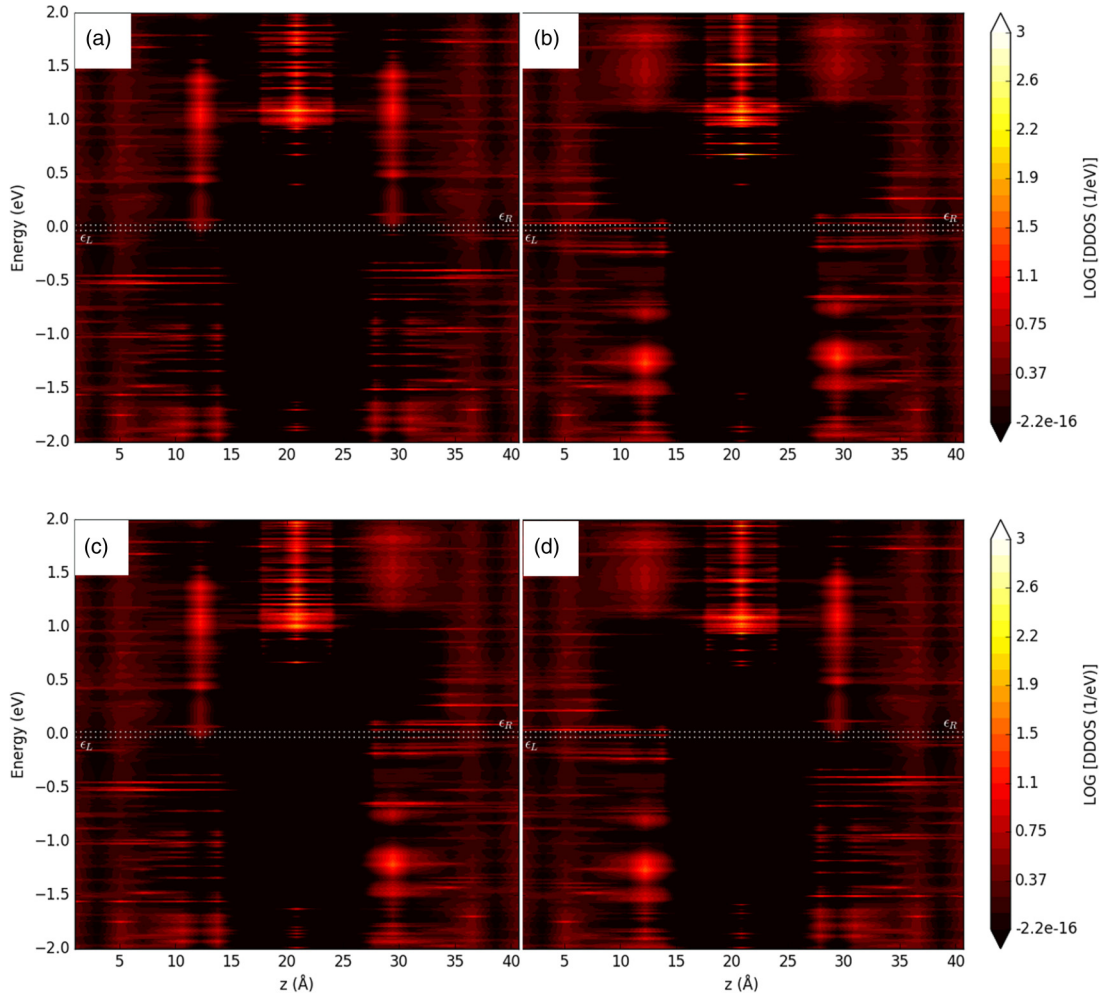

FIG. 6. PLDOS of the majority and minority spin under PC (a), (b) and APC (c), (d) at 0.05 V. The horizontal axis represents different locations of z axis of the device and the vertical axis represents electron energy. Red color indicates high density of states. The dashed white line represents Fermi level of left electrode (ϵ_L) and right electrode (ϵ_R).

Fermi level at both CrI_3 layers are much smaller; therefore, the electron tunneling should be much weaker. For the case of APC shown in Figs. 6(c)–6(d), the DOS is either very small on the right or very small on the left, and the tunneling barrier is very high. As a result, we could get a similar conclusion with Fig. 4 that there are strong TMR effects under finite biases, which is consistent with the currents in Fig. 5.

IV. CONCLUSIONS

In conclusion, we report a 2D van der Waals MTJ based on $MoSi_2N_4$ as tunnel barrier and CrI_3 as ferromagnetic layers with Ag electrodes, which could reach a giant TMR over $10^5\%$. We analyze the transmission spectra and projected band structures to reveal the mechanism of the giant TMR and make a comparison with hBN, graphene barrier, and no barrier. The results suggest that only Δ_5 electrons of majority spin under parallel magnetization configuration could tunnel with high probability in $Ag/CrI_3/MoSi_2N_4/CrI_3/Ag$, resulting in the giant TMR. Diagrams of projected local density of states are also provided to support the conclusion. At last, the working performance of the MTJ under different voltages has been calculated by NEGF approach; it turns out that the MTJ has a giant TMR over $10^5\%$ at zero bias, remains a high TMR about $10^4\%$ below 0.1 V, and remains about 3000% at 0.25 V. It also has a good SIE over 90% below 0.25 V. Our results propose a vertical MTJ with giant TMR, and reveal the potential of $MoSi_2N_4$, a stable 2D material at room temperature, to be a tunnel barrier in MTJs in the future.

ACKNOWLEDGMENT

This work was financially supported by the National Natural Science Foundation of China (Grants No. 11904360, No. 12004375 and No. 12104448).

[1] G. Fuchs, I. Krivorotov, P. Braganca, N. Emley, A. Garcia, D. Ralph, and R. Buhrman, Adjustable spin torque in magnetic tunnel junctions with two fixed layers, Appl. Phys. Lett. **86**, 152509 (2005).

[2] S. Bhatti, R. Sbiaa, A. Hirohata, H. Ohno, S. Fukami, and S. N. Piramanayagam, Spintronics based random access memory: A review, Mater. Today **20**, 530 (2017).

[3] P. Skirdkov and K. Zvezdin, Spin-torque diodes: From fundamental research to applications, Ann. Phys. (Berlin) **532**, 1900460 (2020).

[4] L. Loong, W. Lee, X. Qiu, P. Yang, H. Kawai, M. Saeys, J. H. Ahn, and H. Yang, Flexible MgO barrier magnetic tunnel junctions, Adv. Mater. **28**, 4983 (2016).

[5] S. Knudde, G. Farinha, D. Leitao, R. Ferreira, S. Cardoso, and P. Freitas, AlO_x barrier growth in magnetic tunnel junctions for sensor applications, J. Magn. Magn. Mater. **412**, 181 (2016).

[6] S. Ikeda, K. Miura, H. Yamamoto, K. Mizunuma, H. Gan, M. Endo, S. Kanai, J. Hayakawa, F. Matsukura, and H. Ohno, A perpendicular-anisotropy CoFeB–MgO magnetic tunnel junction, Nat. Mater. **9**, 721 (2010).

[7] S. Yuasa, T. Nagahama, A. Fukushima, Y. Suzuki, and K. Ando, Giant room-temperature magnetoresistance in single-crystal Fe/MgO/Fe magnetic tunnel junctions, Nat. Mater. **3**, 868 (2005).

[8] M. Piquemal-Banci, R. Galceran, S. Caneva, M.-B. Martin, R. S. Weatherup, P. R. Kidambi, K. Bouzehouane, S. Xavier, A. Anane, F. Petroff *et al.*, Magnetic tunnel junctions with monolayer hexagonal boron nitride tunnel barriers, Appl. Phys. Lett. **108**, 102404 (2016).

[9] B. Huang, G. Clark, E. Navarro-Moratalla, D. R. Klein, R. Cheng, K. L. Seyler, D. Zhong, E. Schmidgall, M. A. McGuire, D. H. Cobden *et al.*, Layer-dependent ferromagnetism in a van der Waals crystal down to the monolayer limit, Nature (London) **546**, 270 (2017).

[10] Y. Deng, Y. Yu, Y. Song, J. Zhang, N. Z. Wang, Z. Sun, Y. Yi, Y. Z. Wu, S. Wu, J. Zhu *et al.*, Gate-tunable room-temperature ferromagnetism in two-dimensional Fe_3GeTe_2, Nature (London) **563**, 94 (2018).

[11] M. Bonilla, S. Kolekar, Y. Ma, H. C. Diaz, V. Kalappattil, R. Das, T. Eggers, H. R. Gutierrez, M.-H. Phan, and M. Batzill, Strong room-temperature ferromagnetism in VSe_2 monolayers on van der Waals substrates, Nat. Nanotechnol. **13**, 289 (2018).

[12] B. Huang, G. Clark, D. R. Klein, D. MacNeill, E. Navarro-Moratalla, K. L. Seyler, N. Wilson, M. A. McGuire, D. H. Cobden, D. Xiao *et al.*, Control of 2D magnetism in bilayer CrI_3, Nat. Nanotechnol. **13**, 544 (2018).

[13] T. Song, X. Cai, W. Y. Tu, X. Zhang, B. Huang, N. Wilson, K. Seyler, L. Zhu, T. Taniguchi, K. Watanabe *et al.*, Giant tunneling magnetoresistance in spin-filter van der Waals heterostructures, Science **360**, 1214 (2018).

[14] C. Chen, B. Chao, and W. J. Hsueh, Huge magnetoresistance in graphene-based magnetic tunnel junctions with superlattice barriers, J. Phys. D: Appl. Phys. **48**, 335004 (2015).

[15] P. U. Asshoff, J. L. Sambricio, A. P. Rooney, S. Slizovskiy, A. Mishchenko, E. W. Hill, A. M. Rakowski, A. K. Geim, S. J. Haigh, V. I. Fal'ko *et al.*, Magnetoresistance of vertical Co-graphene-NiFe junctions controlled by charge transfer and proximity-induced spin splitting in graphene, 2D Mater. **4**, 031004 (2017).

[16] M. Piquemal-Banci, R. Galceran, M.-B. Martin, F. Godel, A. Anane, F. Petroff, B. Dlubak, and P. Seneor, 2D-MTJs: Introducing 2D materials in magnetic tunnel junctions, J. Phys. D: Appl. Phys. **50**, 203002 (2017).

[17] Y.-L. Hong, Z. Liu, L. Wang, T. Zhou, W. Ma, C. Xu, S. Feng, L. Chen, M.-L. Chen, D. Sun *et al.*, Chemical vapor deposition of layered two-dimensional $MoSi_2N_4$ materials, Science **369**, 670 (2020).

[18] Q. Wu and L. K. Ang, Giant tunneling magnetoresistance in atomically thin $VSi_2N_4//MoSi_2N_4/VSi_2N_4$ magnetic tunnel junction, Appl. Phys. Lett. **120**, 022401 (2022).

[19] S. Smidstrup, T. Markussen, P. Vancraeyveld, J. Wellendorff, J. Schneider, T. Gunst, B. Verstichel, D. Stradi, P. A. Khomyakov, U. J. Vej-Hansen *et al.*, QuantumATK: An integrated platform of electronic and atomic-scale modelling tools, J. Phys.: Condens. Matter **32**, 015901 (2020).

[20] M. Brandbyge, J.-L. Mozos, P. Ordejon, J. Taylor, and K. Stokbro, Density-functional method for nonequilibrium electron transport, Phys. Rev. B **65**, 165401 (2002).

[21] J. P. Perdew, K. Burke, and M. Ernzerhof, Generalized Gradient Approximation Made Simple, Phys. Rev. Lett. **77**, 3865 (1997).

[22] G. Kresse and J. Furthmüller, Efficient iterative schemes for ab initio total-energy calculations using a plane-wave basis set, Phys. Rev. B **54**, 11169 (1996).

[23] L. Pan, L. Huang, M. Zhong, X. Jiang, H.-X. Deng, J. Li, J.-B. Xia, and Z. Wei, Large tunneling magnetoresistance in magnetic tunneling junctions based on two-dimensional CrX_3 (X = Br, I) monolayers, Nanoscale **10**, 22196 (2018).

[24] J. F. Dillon Jr. and C. E. Olson, Magnetization, resonance, and optical properties of the ferromagnet CrI_3, J. Appl. Phys. **36**, 1259 (1965).

[25] W.-B. Zhang, Q. Qu, P. Zhu, and C.-H. Lam, Robust intrinsic ferromagnetism and half semiconductivity in stable two-dimensional single-layer chromium trihalides, J. Mater. Chem. C. **3**, 12457 (2015).

[26] H. Wang, V. Eyert, and U. Schwingenschlögl, Electronic structure and magnetic ordering of the semiconducting chromium trihalides $CrCl_3$, $CrBr_3$, and CrI_3, J. Phys.: Condens. Matter **23**, 116003 (2011).

[27] See Supplemental Material at http://link.aps.org/supplemental/10.1103/PhysRevB.106.104429 for the band structures of hBN/graphene barrier, transmission spectra of MTJ with monolayer hBN/graphene barrier and without barrier, and PLDOS diagrams of -based MTJ at 0.10-, 0.15-, and 0.20-V biases.

[28] Y. Feng, Z. Cheng, and X. Wang, Extremely large non-equilibrium tunnel magnetoresistance ratio in CoRhMnGe based magnetic tunnel junction by interface modification, Front. Chem. **7**, 550 (2019).

[29] P. Zhao, J. Li, H. Jin, L. Yu, B. Huang, and Y. Dai, Designing lateral spintronic devices with giant tunnel magnetoresistance and perfect spin injection efficiency based on transition metal dichalcogenides, Phys. Chem. Chem. Phys. **20**, 10286 (2018).